Wear 494–495 (2022) 204276

Contents lists available at ScienceDirect

Wear

journal homepage: www.elsevier.com/locate/wear

Unravelling the combined effect of cooling rate and microalloying on the microstructure and tribological performance of $Cu_{50}Zr_{50}$

A. Younes [a], H. Izadi-Gonabadi [b], R. Martínez Sánchez [c], S.J. Bull [b], S. González [a,*]

[a] Faculty of Engineering and Environment, Northumbria University, Newcastle Upon Tyne, NE1 8ST, UK
[b] Newcastle University, School Engineering, Newcastle Upon Tyne, NE1 7RU, UK
[c] Centro de Investigación en Materiales Avanzados (CIMAV), Laboratorio Nacional de Nanotecnología, Miguel de Cervantes No. 120, 31109, Chihuahua, Chih, Mexico

ARTICLE INFO

Keywords:
SEM
Surface roughness
Hardness
Abrasive wear
Delamination wear

ABSTRACT

The combined effect of the cooling rate and microalloying has been studied from suction casted $Cu_{50}Zr_{50}$, $Cu_{49.5}Zr_{50}Fe_{0.5}$ and $Cu_{49}Zr_{50}Fe_1$ at. % rods of 2 mm and 4 mm diameter. For the 2 mm samples, ~1000 K/s cooling rate, the microstructure mostly consists of B2 CuZr austenite and it is basically the same for all compositions. However, 0.5 at. % Fe addition promotes the formation of stress-induced B19' martensite upon wear testing thus improving the wear resistance of the alloy. For the 4 mm samples, ~250 K/s cooling rate, a multiphase intermetallic is predominant and when microalloyed with 0.5 at. % Fe, a relatively large volume fraction of as-cast B33 CuZr martensite is formed thus resulting in a reduction of the wear resistance. At high cooling rate the wear mechanism is predominantly delamination wear while for low cooling rate the large continuous grooves are indicative of abrasive wear.

1. Introduction

Shape Memory Alloys (SMAs) are used in many industries, including the aerospace and automotive sector and in control systems [1–4] due to their desirable characteristics, including shape memory behaviour [5]. This behaviour is characterized by their ability to return to their original shape when heated up above a critical temperature after being subjected to an external force high enough to plastically deform the material in a process called stress-induced martensitic transformation [6]. Among all SMAs, NiTi alloy has been the most popular one due to its superior strength, ductility and high recovery ratio [7]. However, its low transformation temperature and high nickel content as well as the relatively high cost of titanium has limited its use. For this reason, other types of SMAs such as those corresponding to the CuZr system are often viewed as a potential replacement despite their inferior performance and brittleness [7,8]. As in other SMAs, the CuZr system exhibits martensitic transformation when subjected to an external force beyond a threshold value [9–11]. This leads to the transformation from B2 CuZr austenite into B19' CuZr martensite, by a diffusion-less reversible transformation attributed to the fact that martensite can revert into austenite when heated up beyond the austenite finish temperature [12]. An effective method to promote the martensitic transformation for CuZr SMAs is to introduce microalloying elements that can remain in solid solution in the B2 CuZr austenite phase [13]. Among all microalloying elements investigated [14], Fe is one of the most efficient at decreasing the Stacking Fault Energy (SFE) of B2 CuZr, thus promoting the martensitic transformation and work-hardening. The nature and size of the crystalline phase present depends on the cooling rate, which also have an effect on the mechanical performance of the alloys [15]. For example, Nishida and Kainuma [16–18] reported that a decrease of the cooling rate increases the volume fraction of crystalline phases, including the intermetallic compounds Ni_4Ti_3 and Ni_3Ti [19,20]. Similarly, for the CuZr system, a decrease in the cooling rate can lead to the formation of the equilibrium phases $Cu_{10}Zr_7$ and $CuZr_2$ [21–23]. The formation of $Cu_{10}Zr_7$ and $CuZr_2$ can also be promoted by changes in composition. In fact, it was determined that changes as small as ±2 at. % Cu content strongly influence the microstructure and therefore the mechanical performance [24,25].

Although there are some publications about the effect of microalloying on the wear performance of the CuZr system, the combined effect of cooling rate and microalloying has never been explored in detail previously. This is a scientifically and industrially relevant topic since potential synergistic effects of cooling rate and microalloying can lead to the formation of phases and microstructures that cannot be

* Corresponding author.
E-mail address: sergio.sanchez@northumbria.ac.uk (S. González).

https://doi.org/10.1016/j.wear.2022.204276
Received 18 November 2021; Received in revised form 21 January 2022; Accepted 2 February 2022
Available online 5 February 2022

achieved by microalloying alone. From a technological point of view, understanding phase formation is useful for the development of micro-actuators subjected to wear such as those used as temperature-adaptive shaft seals and for space applications (such as spaceships), where very smooth movements are required, and the production of detrimental dust must be limited. The development of these novel cost-effective materials with enhanced performance is expected to compete with polymer seals more effectively and, for general actuator applications, replace costly NiTi Shape Memory Metallic Alloys. From the point of view of the counterbody, stainless steel and nonferrous materials are widely used for sliding rolling applications where low friction is required. Stainless steel resistance to oxidation and staining makes it an ideal material for many applications where temperature reaches high values such as in automotive applications and under direct sunlight for long period of times in the case of satellite applications. SS304 stainless steel was chosen for this study due to its high maximum service temperature in dry air reaching 925 °C [26].

2. Materials and methods

Alloy ingots of nominal composition $Cu_{50}Zr_{50}$, $Cu_{49.5}Zr_{50}Fe_{0.5}$ and $Cu_{49}Zr_{50}Fe_{1}$ (at. %) were prepared by arc melting a mixture of pure elements (>99.9 at. %) in a Ti-gettered high purity argon atmosphere. The master alloys were remelted (heated to a red heat) multiple times to achieve chemically homogeneous ingots. Rod samples of 2 mm and 4 mm diameter were obtained from the master alloy by cooled copper mould casting in an inert gas atmosphere and cooling system set to 20 °C. The structure of the as-cast samples was studied by a SmartLab Rigaku XRD diffractometer with monochromated Cu Kα radiation (25° – 90° range). The Vickers hardness was measured on a WILSON VH1150 test instrument with an indentation load of 3 N and a holding time of 10 s. The hardness values were the average of at least 5 measurements. The microstructure was revealed by etching using Kroll's reagent (2 ml HF, 6 ml HNO_3, and 92 ml H_2O) before being further investigated by scanning and transmission electron microscopy (SEM and TEM). Dry sliding wear experiments were conducted using a pin-on disc tester (DUCOM Micro POD) in air at room temperature following the ASTM-G99 standard. The pins were made by cutting the as-cast rods transversely and the resulting cross-sections were ground to have a flat surface by using 4000 grit paper. Subsequently, the flat surfaces of the pins were wear tested against a flat counterbody disc of 60 HRC hardened SS304 stainless steel of 0.6 mm (R_a) surface roughness provided by the DUCOM company. Tests were performed at increasing loads of 1, 5, 10 and 15 N at a sliding velocity of 0.5 m/s for a sliding distance of 1800 m (i.e., for 1 h). The pin length loss is the average of at least 3 samples and was obtained by measuring the weight of the pins before and after wear tests using an

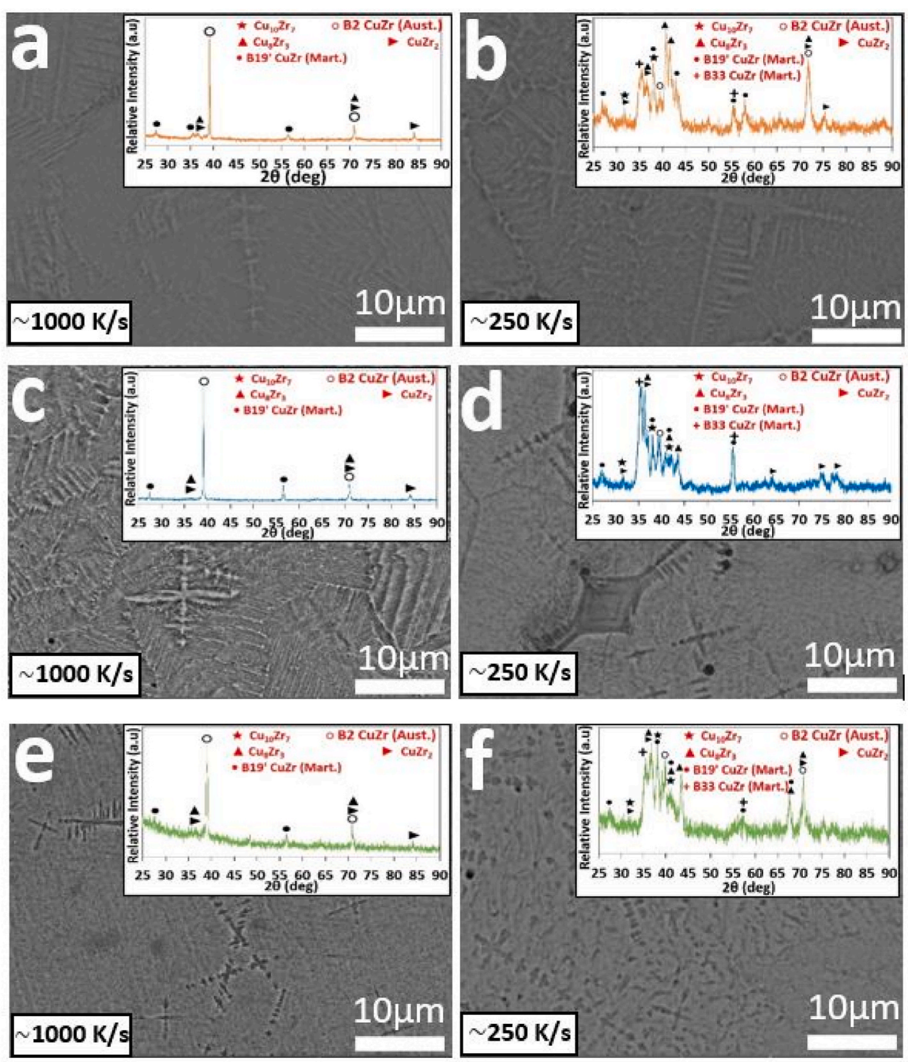

Fig. 1. Backscattered SEM images for 2 mm (~1000 K/s) and 4 mm diameter (~250 K/s) as-cast: (a) and (b) $Cu_{50}Zr_{50}$; (c) and (d) $Cu_{49.5}Zr_{50}Fe_{0.5}$; (e) and (f) $Cu_{49}Zr_{50}Fe_{1}$ samples. The insets show the corresponding general XRD scans from the full cross-section of the sample. Note: The SEM images are taken from the middle radius to be representative.

analytical balance (Fisherbrand™ Analytical Balance, ±0.1 mg) and from the alloy densities. The average roughness and surface profile were analysed using an Alicona InfiniteFocus 3D profilometer and the profiles were obtained by averaging 5 measurements.

3. Results

3.1. Microstructural characterization

The combined effect of the cooling rate and microalloying on the microstructure has been studied by suction casting samples of 2 mm and 4 mm diameter of $Cu_{50}Zr_{50}$, $Cu_{49.5}Zr_{50}Fe_{0.5}$ and $Cu_{49}Zr_{50}Fe_1$ (at. %). The cooling rate, $\dot{T}$, can be estimated from the relationship [27]:

$$\dot{T}(\frac{K}{s}) = \frac{10}{R^2}(\frac{1}{cm^2}) \tag{1}$$

where R is the sample radius; hence for the 2 mm sample the cooling rate is ~1000 K/s while for 4 mm it is ~250 K/s. Fig. 1 shows the backscattered SEM images from a representative area from the sample centre and XRD scans for the 2 mm and 4 mm diameter $Cu_{50}Zr_{50}$, $Cu_{49.5}Zr_{50}Fe_{0.5}$, $Cu_{49}Zr_{50}Fe_1$ SMAs.

The microstructures of the high cooling rate as-cast $Cu_{50}Zr_{50}$ (Fig. 1a), $Cu_{49.5}Zr_{50}Fe_{0.5}$ (Fig. 1c) and $Cu_{49}Zr_{50}Fe_1$ (Fig. 1e) SMAs are very similar and basically consist of dendrites embedded in a fine matrix. To identify the nature of the phases present, XRD scans for the $Cu_{50}Zr_{50}$, $Cu_{49.5}Zr_{50}Fe_{0.5}$ and $Cu_{49}Zr_{50}Fe_1$ SMAs have been performed and are shown as insets in Fig. 1a. They consist of large intensity peaks at 39.4° and 70.8° attributed to cubic B2 CuZr austenite, smaller intensity peaks corresponding to monoclinic B19' and multiple small peaks for the intermetallics Cu_8Zr_3 and $CuZr_2$. This indicates that for the high cooling rate of ~1000 K/s, the retained metastable austenite is the dominant phase.

From EDX studies of the intermetallic phases, Fe was not detected the element but was detected inside the austenite/martensite dendrites, thus suggesting that Fe is present in solid solution as will be discussed later.

The backscattered SEM images and XRD scans for the low cooling rate $Cu_{50}Zr_{50}$ (Fig. 1b), $Cu_{49.5}Zr_{50}Fe_{0.5}$ (Fig. 1d), and $Cu_{49}Zr_{50}Fe_1$ (Fig. 1f) alloys were also obtained for comparison. The microstructure from the middle of the as-cast samples is similar for all the compositions and consists of a combination of dendrites embedded in a matrix of fine microstructure. Compared to the higher cooling rate sample, XRD scan shows much higher intensity peaks from the Cu_8Zr_3 and $CuZr_2$ intermetallic phases and the B19′ CuZr phase (a = 3.2961 Å, b = 4.1937 Å, c = 5.2122 Å), and lower intensity peaks from the B2 CuZr phase (a = 3.2706 Å, b = 3.2706 Å, c = 3.2706 Å) as well as new peaks corresponding to the intermetallic $Cu_{10}Zr_7$ and B33 CuZr martensite (a = 3.2573 Å, b = 4.1143 Å, c = 10.3765 Å). Therefore, when the cooling rate decreases from 1000 K/s to 250 K/s, a microstructure is produced at closer to equilibrium conditions with the formation of more stable phases. The finding of the more stable B33 phase with the Cmcm space group rather than the B2 phase is consistent with the observations of other authors [28]. Despite the microstructural similarities between the $Cu_{50}Zr_{50}$, $Cu_{49.5}Zr_{50}Fe_{0.5}$ and $Cu_{49}Zr_{50}Fe_1$ compositions, some slight differences are noted for $Cu_{49.5}Zr_{50}Fe_{0.5}$. For this intermediate composition, the relative intensity of the XRD peaks at 36.1° and 55.6° (associated with stable B33 martensite) is about twice that of the other two compositions while the intensity of XRD peaks for B19' practically does not change. This indicates that the formation of the B33 phase is synergistically stabilized by the combined effect of reducing the cooling rate and adding 0.5 at. % Fe. Moreover, no peaks from crystalline phase(s) containing Fe are detected, even when the concentration is as high as 1 at. % Fe, thus suggesting the element Fe remains in solid solution even for the lowest cooling rate. These results provide information about the crystallization sequence upon cooling, with retention of the initial metastable B2 austenite at the high cooling rate while at lower cooling rate martensite and intermetallic phases are formed and grow. One should note that the solidification process does not follow the equilibrium diagram [29] especially when the highest cooling rate is achieved since practically no equilibrium intermetallic phases are present.

Since the presence of Fe in solid solution and its concentration is key in the formation of a stress-induced phase, the retention of this element upon cooling in the dendrites of the samples cooled at ~1000 k/s and ~250 K/s has been studied. Backscattered SEM images and EDX scans have been obtained from the dendrites close to the centre of the sample (i.e., where the cooling rate is the slowest and thus dendrites are prone to highest segregation). The dendrites for the high cooling rate $Cu_{50}Zr_{50}$, $Cu_{49.5}Zr_{50}Fe_{0.5}$ and $Cu_{49}Zr_{50}Fe_1$ samples and corresponding EDX scans from the centre of each dendrite (i.e., point indicated by the red arrow) are shown in Fig. 2a, Fig. 2c and e, respectively. Similarly, for the low cooling rate sample, EDX scans have been taken from the inner part of the dendrites as indicated in Fig. 2b, d and f. The red arrows point towards a region close to centre of each dendrite from where the EDX results were taken and summarized in the inset table for each panel. For the three compositions, the concentration of Cu and Zr are relatively similar, thus confirming that the dendrites correspond to austenite B2 CuZr and B19' martensite. The clear halo around the dendrites suggest that this area is rich in the element of higher atomic weight, Zr (91.224), thus leaving the dendrites slightly richer in the element of lower atomic weight, Cu (63.546). These differences in intensity agree with the EDX results. The composition profile of the dendrite/matrix interface is associated with the classical nucleation and growth mechanism for which the solute is transported down a composition gradient toward the dendrite [30]. EDX results indicate that the concentration of the Fe microalloying element inside the dendrites is 0.3 at. % for $Cu_{49.5}Zr_{50}Fe_{0.5}$ and 0.9 at. % for $Cu_{49}Zr_{50}Fe_1$, which are very close to the nominal composition of the alloys thus suggesting that Fe remains in solid solution. In fact, Fe is retained even for the slowest cooling rate, i.e., at the centre of the 4 mm diameter sample, the concentration of Fe measured by EDX is 0.5 and 1 at. % for $Cu_{49.5}Zr_{50}Fe_{0.5}$ and $Cu_{49}Zr_{50}Fe_1$ alloys, respectively.

In order to investigate the nano-matrix of the casted alloys, TEM images have been obtained for $Cu_{50}Zr_{50}$ of 2 and 4 mm samples as shown in Fig. 3. Despite investigating the dendrites of 2 and 4 mm samples in Fig. 2, it is not possible to assess the size of grains embedded in the crystalline matrix using SEM, therefore TEM images were taken. Fig. 3a shows a representative area of as cast 2 mm $Cu_{50}Zr_{50}$ with grains embedded in the crystalline matrix, the arrows pointed towards grains that may reach 70 nm in size. Similarly, Fig. 3b shows a representative area of as cast 4 mm $Cu_{50}Zr_{50}$ where size of grains visibly distinguished by colour tonality difference are larger than that reported for 2 mm sample.

3.2. Wear behaviour

3.2.1. Pin-on-disc test

To investigate the combined effect of cooling rate and microalloying on the wear performance, pin-on-disc tests have been performed. Fig. 4 shows the wear expressed as pin length loss for the three different compositions $Cu_{50}Zr_{50}$, $Cu_{49.5}Zr_{50}Fe_{0.5}$ and $Cu_{49}Zr_{50}Fe_1$ and diameters of 2 mm (~1000 k/s) and 4 mm (~250 k/s) when tested at 5, 10 and 15 N applied for 1 h and also 40 N for the 4 mm sample. The 40 N test is performed to achieve the same pin-disc normal contact pressure (P = 3.2 MPa) as in the 2 mm sample under 10 N load. When the high cooling rate sample is subjected to a testing load of 15 N, a normal contact pressure of 4.8 MPa is achieved.

The pin length loss for the high cooling rate samples is very similar for all compositions when a load of 5 N is applied. However, when 10 and 15 N load are applied, the length loss depends on the composition. The lowest value is achieved at both loads for the $Cu_{49.5}Zr_{50}Fe_{0.5}$ alloy but is similar for the other compositions (i.e., $Cu_{50}Zr_{50}$ and $Cu_{49}Zr_{50}Fe_1$). This indicates that addition of 0.5 at. % Fe enhances the wear resistance

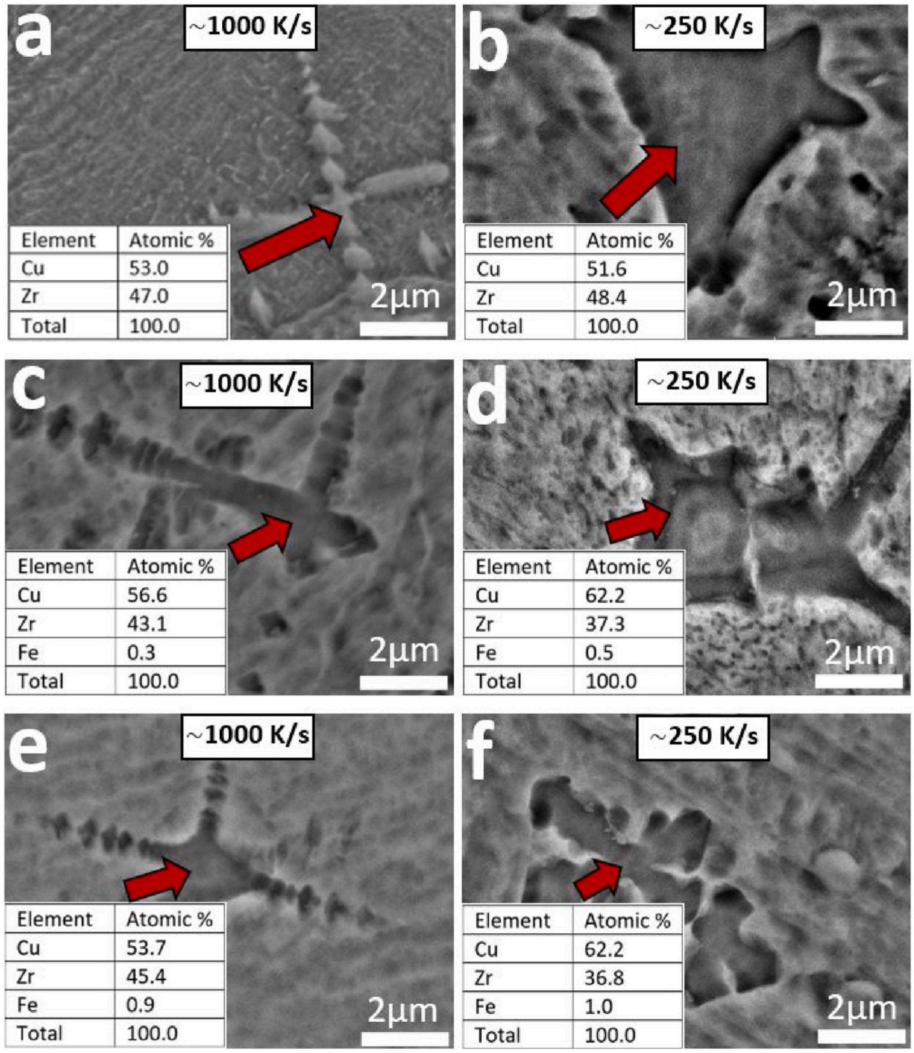

Fig. 2. Magnified Backscattered SEM images from the dendrites located in the centre of 2 mm (~1000 k/s) and 4 (~250 k/s) mm samples: (a) and (b) $Cu_{50}Zr_{50}$; (c) and (d) $Cu_{49.5}Zr_{50}Fe_{0.5}$; (e) and (f) $Cu_{49}Zr_{50}Fe_1$ samples. The red arrows show the point at the centre of each dendrite from where the EDX results summarized in the inset tables were taken. (For interpretation of the references to colour in this figure legend, the reader is referred to the Web version of this article.)

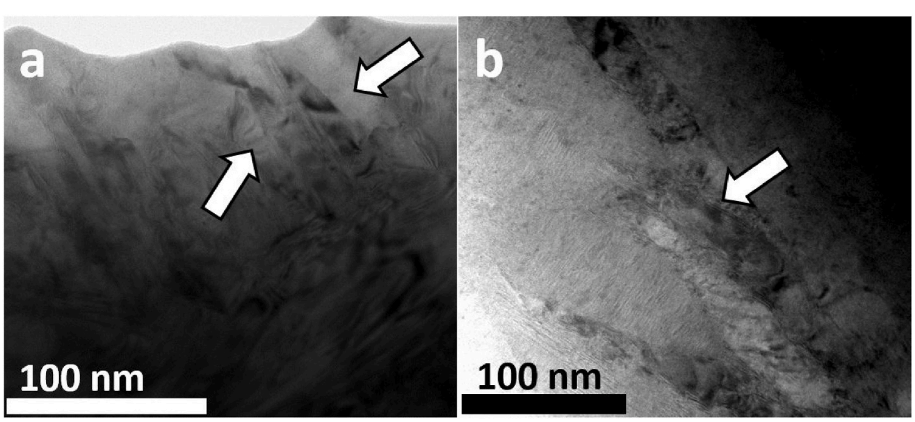

Fig. 3. Bright field TEM image of (a) as-cast 2 mm (~1000 k/s) $Cu_{50}Zr_{50}$ and (b) as-cast 4 mm (~250 k/s) $Cu_{50}Zr_{50}$. The white arrows points towards grains embedded in crystalline matrix.

of the $Cu_{50}Zr_{50}$ alloy but only when the load is at least of 10 N thus suggesting that a stress sensitive mechanism is responsible for this behaviour. The wear resistance enhancement is attributed to the work hardening that B2 austenite experiences when it is transformed into martensite upon loading [13]. When the 2 mm pin is subjected to 10 N load, the pin-disc contact pressure is about 3.2 MPa. This is estimated to be the minimum pressure required to transform B2 austenite into B19′ martensite. This transformation is promoted by the presence of 0.5 at. %

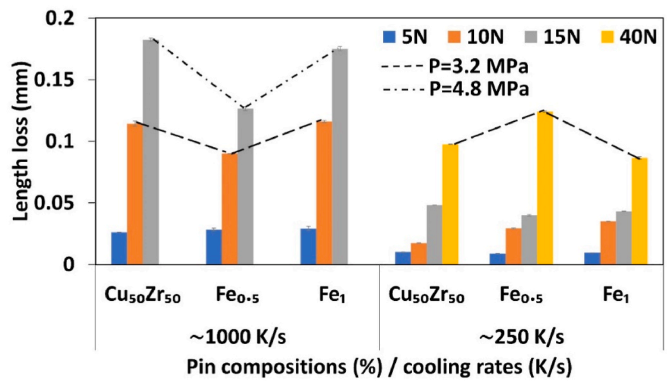

Fig. 4. Evolution of pin length loss for 2 mm (~1000 k/s) and 4 mm (~250 k/s) for the different alloys: $Cu_{50}Zr_{50}$, $Cu_{49.5}Zr_{50}Fe_{0.5}$ and $Cu_{49}Zr_{50}Fe_1$ for 5, 10 and 15 N loads applied for 1 h. Results for 40 N is also included.

Fe in solid solution (Fig. 2), which is consistent with observations from Wu et al. [14]. According to these authors, partial replacement of Cu from B2–CuZr phase by 0.5 at. % Fe decreases the SFE from 381 mJ/m^2 to ~125 mJ/m^2. However, further addition of Fe to 1 at. % does not seem to promote the martensitic transformation of CuZr austenite since the wear resistance is the same as that of the $Cu_{50}Zr_{50}$ alloy. For the low cooling rate samples (Fig. 4), the pin length loss for 15 N is similar for all compositions. This is expected to be due to not only to microstructural differences resulting from the lower cooling rate but also to the lower pin-disc contact pressure leading to reduced stress-induced transformation; the cross-section area for the 4 mm diameter pin (12.57 mm^2) is larger than for the 2 mm diameter pin (3.14 mm^2). To achieve the same pressure as on the 2 mm pin subjected to 10 N load with the 4 mm sample, a 40 N load is required and therefore wear tests at this pressure for 1 h have been also conducted (Fig. 4). For the low cooling rate samples under 40 N load, the length loss for $Cu_{50}Zr_{50}$ and $Cu_{49}Zr_{50}Fe_1$ are similar, 0.097 mm and 0.086 mm respectively, while for $Cu_{49.5}Zr_{50}Fe_{0.5}$ it is the highest, i.e., 0.124 mm, i.e., lowest wear resistance. This behaviour is therefore opposite to that observed in the high cooling rate samples and could be explained by the microstructural differences. A high volume fraction of hard and therefore wear resistant intermetallic phases are present in $Cu_{50}Zr_{50}$ and $Cu_{49}Zr_{50}Fe_1$ alloys (Fig. 1 and [31]. However, for the low cooling rate $Cu_{49.5}Zr_{50}Fe_{0.5}$ alloy, in addition to these intermetallic phases, a high concentration of the B33 CuZr martensite phase is also present, which is different from the stress-induced martensite B19' produced by twinning in the high cooling rate sample. These results suggest that B33 CuZr is a low wear resistance phase. The reason for this behaviour will be investigated in more detail in the future.

The contact pressure measured in this study in Fig. 4 ranges from 3.2 to 4.8 MPa, which are of a similar order of magnitude to those previously reported by Phinney et al. [32]. Additionally, our values also match those reported by Ng et al. [33] where contact pressure was 2 MPa for near-equiatomic NiTi alloy.

3.2.2. Hardness tests

To better understand the combined effect of cooling rate and microalloying on the wear performance, hardness tests have been performed. It is well known that the total wear volume produced is expected to be inversely proportional to the hardness (for a given material system) as indicated by Archard's equation [34]:

$$Q = \frac{KLD}{H} \tag{3}$$

where Q is the volume of wear debris produced (volumetric loss), K is the wear coefficient, a dimensionless constant taken as 6.23×10^{-4} for our case [35], L the load normal to the surface, D the sliding distance and H the hardness of the softer material of the contacting surfaces. For this reason and in order to corroborate our wear tests results, hardness measurements were made at high enough load (3 N) do that the plastic zone around the indentation would include all the crystalline phases to get a representative value for the microstructure as a whole. Measurements were done along the radius of the 2 and 4 mm samples for the 3 compositions as shown in the schematic in Fig. 5 from the centre to the edge. The effect of the composition and distance from the centre is small, ranging from about 2.30 to 3 GPa for the 2 mm sample while for the 4 mm sample it ranges from about 3 to 3.74 GPa. This suggests that the difference in cooling rate due to a change in diameter has much higher effect on the hardness. To better highlight this, the hardness versus the variation in the concentration of Fe added for both diameters has been plotted. While for the 2 mm sample highest hardness of about 3 GPa is attained for the $Cu_{49.5}Zr_{50}Fe_{0.5}$ alloy, the 4 mm sample shows the lowest value, about 3.46 GPa. These values are similar to those previously reported for CuZr-based alloys [36]. The hardness is consistent with the wear test values (Fig. 4) since the pin length loss for the 2 mm diameter samples is the smallest for $Cu_{49.5}Zr_{50}Fe_{0.5}$ while for the 4 mm diameter samples it is the highest. The results also agree with the XRD scans and SEM images (Figs. 1 and 2) for which mostly hard intermetallic phases ($Cu_{10}Zr_7$, Cu_8Zr_3 and $CuZr_2$) are detected for the low cooling rate samples while for the high cooling rate samples the microstructure is dominated by relatively soft B2 CuZr austenite dendrites(see Fig. 6).

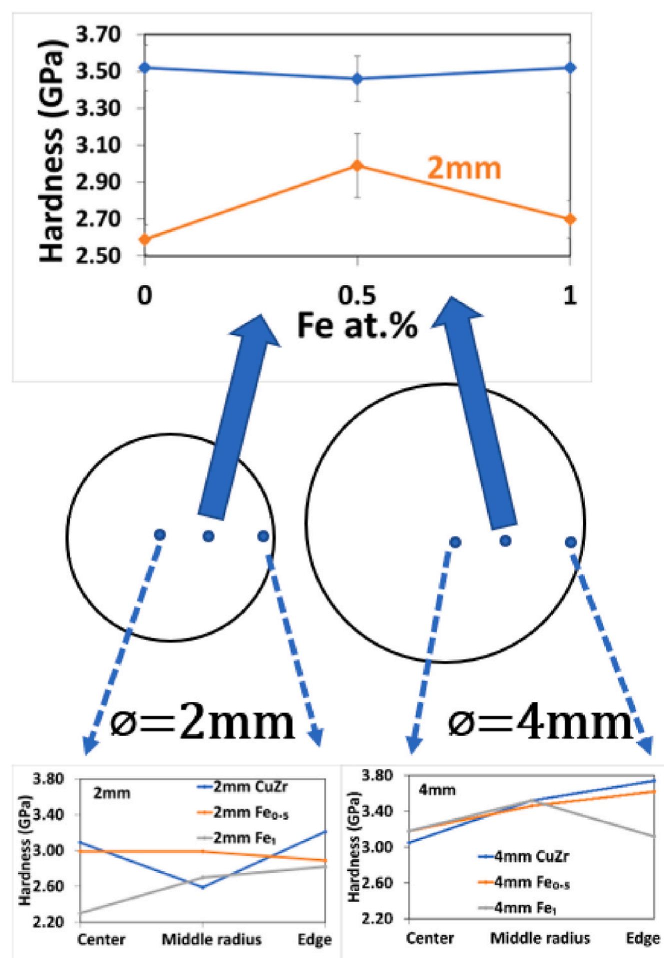

Fig. 5. Schematic showing the 2 mm (~1000 k/s) and 4 mm (~250 k/s) cross section rod samples and locations from where hardness was measured (centre, middle radius, and edge, with centre as origin of the distance) as shown in the plots. The hardness values measured in the middle radius of the 2 mm and 4 mm samples versus the concentration in Fe are also shown.

This is the first time that the effect of the cooling rate on the hardness of the CuZr system has been reported as far as the authors are aware. These results are consistent with the evolution of the hardness with the cooling rate observed by Motemani et al. [17] in NiTi alloys.

3.2.3. Morphological analysis after wear tests

To investigate the effect of the cooling rate on the wear performance in more detail, the worn surface of the $Cu_{49.5}Zr_{50}Fe_{0.5}$ pin of 2 mm diameter (~1000 k/s) tested at 15 N (Fig. 6a, b, 6c and 6d), and the 4 mm diameter (~250 k/s) of the same composition tested at 15 N (Fig. 6e, f, 6g and 6h) and at 40 N load (Fig. 6i, j, 6k and 6l) for 1 h has been characterised. In addition, the debris generated upon wear testing that is attached onto the pin surface has been studied. This composition was selected since it exhibits the highest wear resistance among the 2 mm diameter samples and is a good basis of comparison for the 4 mm diameter samples.

The general images for the high cooling rate (Fig. 6a) and low cooling rate samples (Fig. 6e and i) show continuous grooves throughout the cross-section of the samples caused by ploughing, indicating an abrasive wear mechanism [37]. A load increase from 15 N to 40 N for the low cooling rate samples increases the groove depth; the average roughness increases from $R_a = 0.462$ μm (Fig. 6f) at 15 N to $R_a = 0.533$ μm (Fig. 6j) at 40 N. These values are much higher than the $R_a = 0.200$ μm for the 2 mm sample tested at 15 N (Fig. 6b). This can be attributed to the relatively high content of hard abrasive $Cu_{10}Zr_7$, Cu_8Zr_3 and $CuZr_2$ intermetallic phases present in the wear debris for the low cooling rate sample compared to the high cooling rate sample (SEM and XRD from Fig. 1). This wear debris is rich is oxygen, with concentrations ranging from about 32 to 34 at. % and is therefore significantly oxidised during dry wear. The degree of oxidation does not seem to depend on the load. The Zr to Cu ratio of the wear debris is around 1.15, close to the nominal composition of the $Cu_{50}Zr_{50}$, $Cu_{49.5}Zr_{50}Fe_{0.5}$ and $Cu_{49}Zr_{50}Fe_1$ SMAs and this suggests that the material has not been systematically removed from any single phase but from all phases in the cross-section. This wear debris generates abrasive damage as it slides across the pin surface (Fig. 6e).

However, for the high cooling rate sample, the surface is smoother and free of significant debris (Fig. 6a), thus suggesting lower presence and release of abrasive intermetallic particles, which is consistent with the XRD scans (Fig. 1a, c and e). In general, for two materials with the same phase composition one could expect higher hardness (i.e., higher yield strength) and hence room temperature wear resistance for the sample cooled faster, i.e., 2 mm diameter, due to microstructural refinement. However, differences in cooling rate not only have an effect in the nature but also in the volume fraction of the phases formed. The larger volume fraction of intermetallic crystallites for the 4 mm diameter samples, which are harder than B2 CuZr austenite or B19' and B33 CuZr martensites are responsible for the enhanced wear resistance. Another important difference is that while for the high cooling rate samples subsurface cracks are present (inset of Fig. 6c), no such features are observed for the low cooling rate samples. The presence of these cracks is associated with plastic deformation likely caused by surface fatigue and therefore the contact stress is high enough to transform austenite into martensite. These subsurface cracks propagate subsequently under surface fatigue loading and lead to delamination (i.e., lamellar wear particles) [38] as previously observed in alloys of similar composition

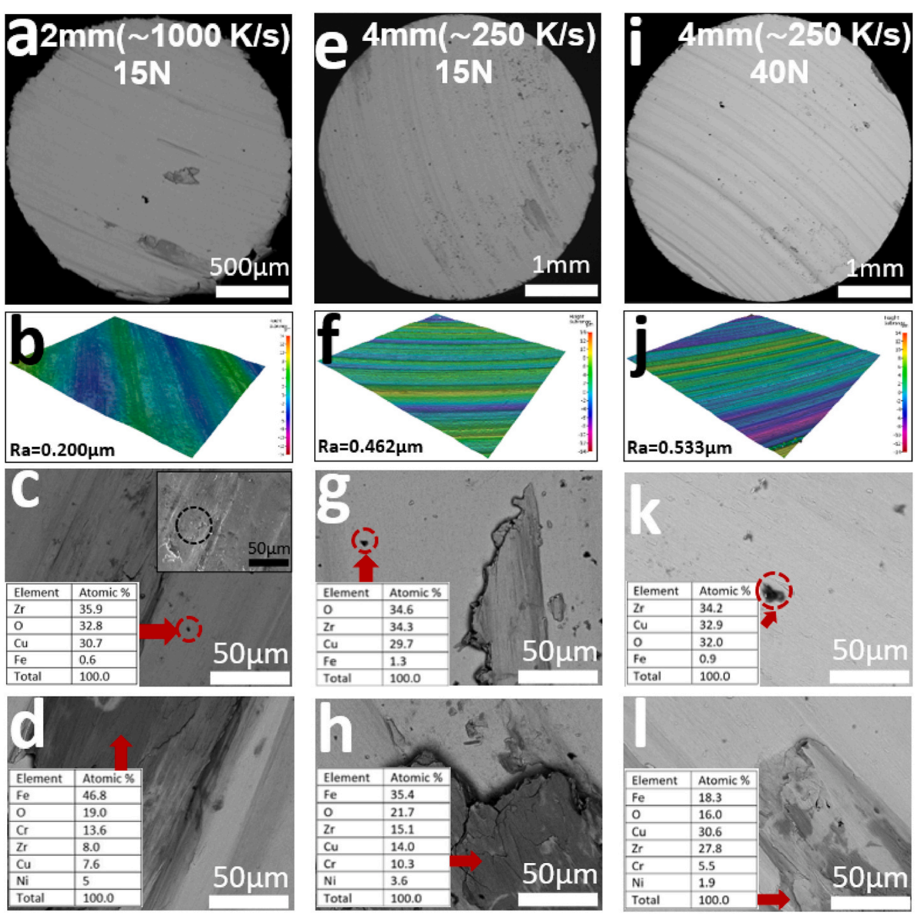

Fig. 6. SEM images from $Cu_{49.5}Zr_{50}Fe_{0.5}$ pin: (a) General image for 2 mm and 15 N load; (b) and (c) details showing dark particles and smeared patches respectively; (d) General image for 4 mm and 15 N load; (e) and (f) details showing dark particles and smeared patches respectively; (g) General image for 4 mm and 40 N load; (h) and (i) details showing dark particles and smeared patches respectively.

(e.g., $Cu_{45.5}Zr_{51}Al_{3.5}$ at. % alloy [39]). These subsurface cracks relate directly to delamination wear mechanism, which is different from abrasive and adhesive wear [40]. The subsurface cracks observed in Fig. 6c are similar to those observed by other authors [41–43] and they were related to surface fatigue. This delamination is responsible for the large amount of material loss displayed by the 2 mm diameter sample (Fig. 4) since in the delamination process larger wear particles are removed compared to that in abrasive wear. However, for the low cooling rate samples, no signs of plastic deformation are observed, and this is associated to the presence of abundant hard and brittle intermetallic phases. Additional features are the wear debris particles (see arrows for Fig. 6c, g and k) and smear patches (evidence of plastic deformation dominated adhesive wear - see arrows for Fig. 6c, f and i) detected on the surface of both samples. These patches are associated with the transfer of SS304 steel from the counterbody disc to the pins and therefore are indicative of adhesive wear of the counterface. The general images from the worn surfaces of the low cooling rate pin tested at 15 N (Figs. 6e) and 40 N (Fig. 6i) show similar features but for 40 N load the roughness is higher and the presence of smeared SS304 steel patches transferred from the disc counterface are rare. Both surfaces exhibit oxides (Fig. 6g and k) from the oxidation of the intermetallic particles released but they do not exhibit the subsurface cracks detected in the high cooling rate samples, thus suggesting that the wear mechanism for the low cooling rate samples is predominantly abrasion rather than delamination, additionally, the abundant presence of hard abrasive intermetallic particles such as $Cu_{10}Zr_7$, Cu_8Zr_3 and $CuZr_2$ contribute greatly towards abrasion being the dominant wear mechanism for low cooling rate. When testing at 40 N, the steel transfer patches attached to the pin are about 3 times richer in Cu and Zr (see EDX from Fig. 6l) than when testing at 15 N (see EDX from Fig. 6h). The Cu and Zr originates from the $Cu_{49.5}Zr_{50}Fe_{0.5}$ pin, which wears out about 3 times more at 40 N than at 15 N load (see length loss in Fig. 4). However, the intermixing of stainless steel with Cu and Zr during transfer is not homogeneous as can be deduced from the areas of different grey colouration of the patch shown in the backscattered SEM image of Fig. 6l. This steel patch contains mostly light grey areas which is due to a high content of elements with relatively high atomic number, Cu (30.6 at. %) and Zr (27.8 at. %) that mix during the wear test thus turning these patches into a composite of stainless steel with Cu and Zr. The patch also contains some isolated darker areas which are richer in chromium and iron, elements of lower atomic number present in the stainless steel, and poorer in Cu and Zr. The low number of patches on the pin surface when testing at 40 N is attributed to the lower ability of these composite patches to attach and spread because they should be more stiff and less ductile than the more Fe-rich patches attached when testing at 15 N load. The reason is that, according to the rule of mixtures, the properties of the composite patches approach to those of the CuZr intermetallic phases as they get richer in intermetallic phases. In this study, abrasive, adhesive and delamination wear features have been observed. Table 1 lists the different wear mechanisms, features observed in each and possible causes.

An important parameter to assess the tribological performance is the coefficient of friction (COF) since it provides information about the resistance encountered when moving one object over another [44]. In many cases, a small value of the COF suggests high wear resistance, i.e., small material loss [45]. During the wear test experiments, the evolution of the COF exhibits two stages. The first stage is unstable and is characterized by a rapid increase of COF for a short time at the start of the test and is associated with establishing the transfer layer and the surface roughness, followed by a second steady state stage which represents most of the duration of the test. Fig. 7 shows the comparison of evolution of COF over time, from 600 to 3600 s, for $Cu_{50}Zr_{50}$, $Cu_{49.5}Zr_{50}Fe_{0.5}$ and $Cu_{49}Zr_{50}Fe_1$ when tested at 15 N load for the 2 mm diameter samples (Fig. 7a) and for the 4 mm diameter samples tested at 15 N (Figs. 7b) and 40 N (Fig. 7c) load.

For high cooling rate samples at 15 N load, the lowest COF is 0.47 and corresponds to the $Cu_{49.5}Zr_{50}Fe_{0.5}$ alloy. This is attributed to the work-hardening effect of the martensitic transformation of B2 CuZr austenite promoted by the presence of Fe in solid solution. For the 4 mm diameter sample at 15 N load (Fig. 7b) the values of the COF are practically the same, which is consistent with the similar wear rate data (Fig. 4). Finally, for the low cooling rate samples tested at 40 N, the $Cu_{49.5}Zr_{50}Fe_{0.5}$ exhibits the highest COF, around 0.53 compared to about 0.48 for $Cu_{50}Zr_{50}$ and $Cu_{49}Zr_{50}Fe_1$. The difference in COF is because when the load increases, the effect of deformation of the microstructure becomes more significant. Since the $Cu_{49.5}Zr_{50}Fe_{0.5}$ alloy contains less intermetallic phases and more easily deformable as-cast

Table 1
Surface morphology features, possible causes and wear mechanism responsible.

Surface morphology features	Possible causes	Wear mechanism responsible
Long continuous grooves	Ploughing	Abrasive wear
Subsurface cracks and sheet-like fragments	Surface fatigue	Delamination wear
Smear patches	Material transfer between counterface and counterbody	Adhesive wear

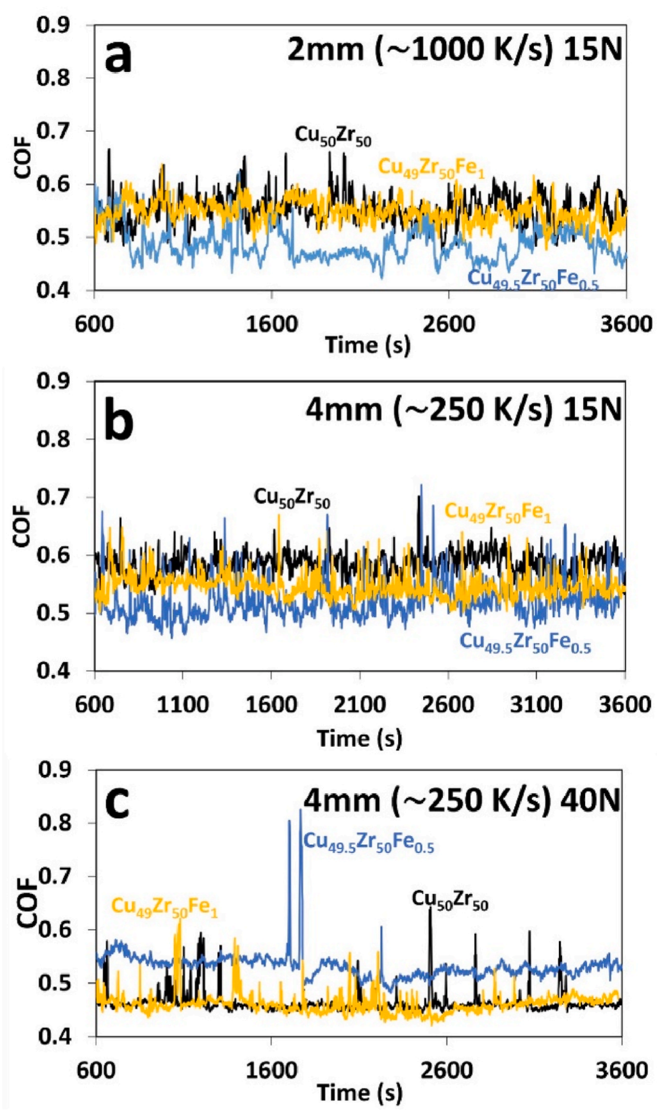

Fig. 7. The COF as a function as a function of the wear time, from 600 to 3600 s during the steady-stage state for the 2 mm (~1000 K/s) and 4 mm (~250 K/s) samples.

B33 martensite than $Cu_{50}Zr_{50}$ and $Cu_{49}Zr_{50}Fe_1$, its COF is higher, i.e., 0.53, and its wear rate (pin length loss, i.e., 0.128 mm) is the highest (Fig. 4). These COF values are close to those reported in the literature, from about 0.4 to 0.6 for $Cu_{60}Zr30Ti_{10}$ at. % [46] and about 0.35–0.45 for a Cu-BMG (bulk metallic glass), of similar composition to the alloys of this work, when sliding against EN26 steel [37].

The correlation between the microstructure and the mechanical performance (wear and hardness) are discussed in more detail here. Typically, faster cooling rate results in a refined microstructure and therefore in an enhancement of the yield strength [47]. At the same time, an increase of the yield strength results in a hardness increase, estimated from Tabor's relationship $\sigma_y = H/3$ and therefore enhancement of the wear resistance. However, this trend is not followed for the $Cu_{50}Zr_{50}$ alloy for three reasons, first because at high cooling rate abundant ductile austenite metastable B2 phase is retained, second because not all materials contain a stress-induced martensite phase associated with work-hardening that can be tuned by microalloying and third because a small decrease of the cooling rate to 250 K/s results in the formation of wear resistant intermetallic phases. After wear testing at 15 N, high cooling rate samples containing 0.5% Fe exhibit work-hardening and martensitic transformation as explained in Fig. 4. The relatively small wear rate of high cooling rate samples of this composition compared to other alloys is attributed to the effect of martensitic transformation. This can be seen from Fig. 8a where an increase in intensity of the XRD peak associated to B19′ martensite (at angle 35.6°) after the wear test is observed compared to the intensity of the same peak in the as-cast condition, before wear testing (Fig. 1c).

XRD scans provide an overall analysis of the microstructure, however, for greater in-depth analysis, TEM has been performed for 2 mm $Fe_{0.5}$ after testing at 15 N load. A bright field TEM image and corresponding Selected Area Electron Diffraction (SAED) pattern from the phase indicated by the arrow show the presence of twinned B19' CuZr martensite. The increase in volume fraction of this phase is responsible for the hardness increase (Fig. 5) and enhanced wear resistance (Fig. 4). In the case of the 4 mm diameter sample with 0.5% Fe, the wear resistance is relatively low due to presence of the B33 martensite phase (at angle 36.1°) in the as-cast condition (Fig. 1d). This can also be observed after testing at 15 N (see XRD of Fig. 8b) where high-volume fraction of B33 and intermetallic phases are present in the worn sample. These results agree with the TEM analysis (inset Fig. 8b) where the $Cu_{10}Zr_7$ intermetallic is detected and indexed.

The B33 martensite phase was previously detected in CuZr alloys by Zhou and Napolitano [28] and they assigned to it a new superstructure (S) with space group Cmcm. However, the effect of B33 phase on the wear and mechanical performance has not been studied before. Our results indicate that when the cooling rate is ~1000 K/s (2 mm diameter pins), no XRD peaks associated to B33 where detected (see Fig. 1a, c and e). On the other hand, when cooling rate drops to ~250 K/s (4 mm diameter pins), XRD peaks of B33 appear in the as-cast condition as can be seen in (Fig. 1b, d and f). This agrees with the observation from Yue et al. [48] where it was found that B33 tends to form and stabilise after structural relaxation, meaning that when cooling rate drops from 1000 K/s to 250 K/s, the chances of formation and stabilization of the B33 phase dramatically increases. The presence of B33 plays an important role in the wear performance of CuZr SMAs. For example, when the pressure on the pin is equivalent for both diameter sizes (i.e., 3.2 MPa) as can be seen in Fig. 4, the pin length loss for 2 mm diameter samples containing 0.5% Fe is 0.09 mm while for 4 mm samples of the same composition is 0.12 mm. The small length loss for the 2 mm samples is attributed to the transformation to the B19′ martensite as can be seen in XRD after testing (see Fig. 8a). Meanwhile, the high pin length loss (0.12 mm) for the 4 mm sample is attributed to the presence of B33 martensite (see Fig. 8b). This is a significant finding since for 4 mm diameter $Cu_{50}Zr_{50}$ and Fe_1 the wear resistance was smaller than for the other two compositions of 2 mm diameter due to the higher volume fraction of the hard intermetallic multiphase. There is also an agreement between the COF and the wear resistance. The $Cu_{50}Zr_{50}$, $Cu_{49.5}Zr_{50}Fe_{0.5}$, and $Cu_{49}Zr_{50}Fe_1$ alloys of Fig. 7 show a clear decrease in COF with increase in hardness (Fig. 5) and wear resistance (Fig. 4). Zhao et al. [49] have investigated the relationship of between wear resistance of NiTi SMAs and COF. It was found that samples that exhibited better wear resistance also exhibited the lowest COF, which agrees with our results. Other researchers [50,51] have also observed the same trend. The correlation between the hardness and wear resistance observed for $Cu_{50}Zr_{50}$, $Cu_{49.5}Zr_{50}Fe_{0.5}$, and $Cu_{49}Zr_{50}Fe_1$ alloys are consistent with Archard's equation [34].

Considering that in sliding wear it is important to analyse the performance of the entire tribosystem, the surfaces of the SS304 counterbody after the wear tests with $Cu_{49.5}Zr_{50}Fe_{0.5}$ have been analysed (Fig. 9).

For the high cooling rate sample tested at 15 N load for 1 h (Fig. 9a) the general image (Fig. 9a) shows a homogeneous distribution of transfer patches across the track width that according to the mapping contain Cu and Zr. This confirms full contact between the pin surface and the disc and therefore the validity of the wear test results. When comparing the surface morphology of the 2 mm samples tested at 15 N (Fig. 9a) with the low cooling rate samples tested at 40 N (Fig. 9c) for $Cu_{49.5}Zr_{50}Fe_{0.5}$, there are larger patches oriented along the track

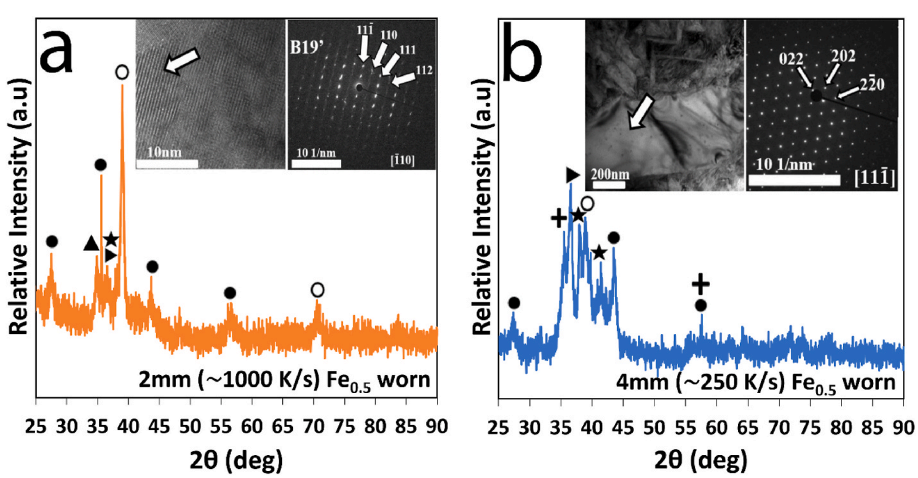

Fig. 8. XRD scan of: (a) 2 mm (~1000K/s); (b) 4 mm diameter (~250K/s) $Fe_{0.5}$ sample after being wear tested at 15 N. Insets show bright field TEM image of a representative area (see arrow) and corresponding SAED pattern: (a) B19′ phase with zone axis [−110]; (b) $Cu_{10}Zr_7$ phase with zone axis [1–11]. Symbols: ★$Cu_{10}Zr_7$, ○B2 CuZr (Aust.), ▲Cu_8Zr_3, ▶$CuZr_2$, ●B19' CuZr (Mart.), + B33 CuZr (Mart.).

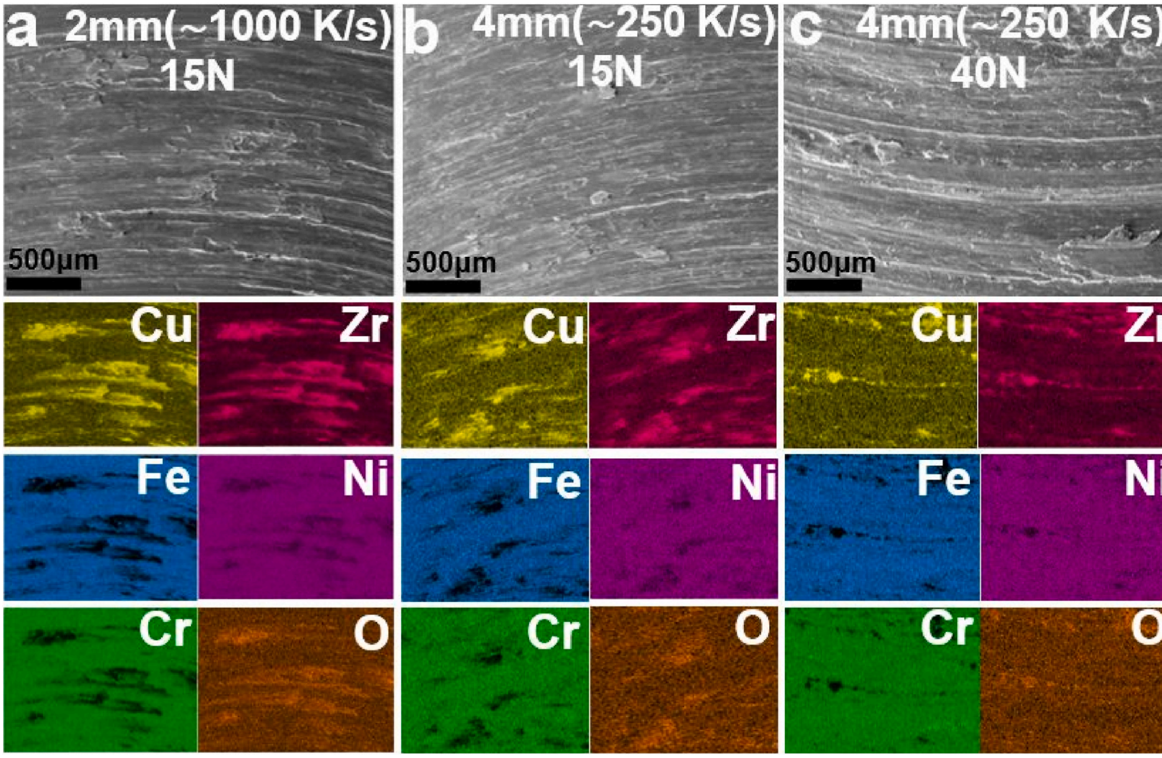

Fig. 9. SEM backscattered image of SS304 counterbody worn disc after testing the $Cu_{49.5}Zr_{50}Fe_{0.5}$ alloy at the following conditions: (a) 2 mm (~1000 K/s) sample at 15 N; (b) 4 mm (~250 K/s) at 15 N; (c) 4 mm (~250 K/s) at 40 N load for 1 h. In addition, the corresponding compositional X-ray mappings for Cu, Zr, Fe, Ni Cr and O are shown.

direction at the lower load. These CuZr patches originate mostly from the B2 CuZr austenite and B19' CuZr martensite dendrites and therefore they are relatively ductile compared to the intermetallic phases and therefore can be easily smeared along the track. For the low cooling rate samples, the higher volume fraction of hard and brittle $Cu_{10}Zr_7$, Cu_8Zr_3 and $CuZr_2$ intermetallic phases make transfer of the CuZr more difficult and reduce its spread on the steel disc thus resulting in more discontinuous round transfer patches at 40 N load than for high cooling rate sample at 15 N test load. The volume fraction of phases in the 2 and 4 mm diameter samples will be further discussed in section 4. The morphology of the disc after testing with the 4 mm diameter pin at 15 N (Fig. 9b) exhibits intermediate features between those of the 2 mm sample at 15 N and 4 mm sample at 40 N.

The results show that microalloying as a strategy to enhance the wear resistance of CuZr shape memory alloys is only useful when the cooling rate is fast enough (~1000 K/s) to attain a microstructure consisting mostly of retained austenite. This microstructure can be useful to develop shape memory components such as microactuators. However, fabrication of these components at a slower cooling rate (250 K/s) would lead to the formation of crystalline phases such as intermetallics that do not show the shape memory effect, and therefore are not useful for microactuator applications. In this work it has been shown that 0.5 at. % Fe addition is useful to enhance the wear resistance of the CuZr SMA obtained at a cooling rate of ~1000 K/s by promoting the transformation of the B2 CuZr austenite into stress-induced B19' CuZr martensite leading to work-hardening. However, partial replacement of Cu by 0.5 at. % Fe has a detrimental effect on the wear resistance when the alloy is obtained at a slower cooling rate of about 250 K/s since in this case the 0.5 at. % Fe promotes the formation of B33 CuZr martensite upon casting, i.e., a phase which is much softer than the stress-induced martensite formed at higher cooling rates.

4. Discussion

4.1. Microstructural analysis

To understand the combined effect of the cooling rate and microalloying on the mechanical performance of CuZr based SMAs, Fig. 10 presents in a simple schematic the microstructures formed upon cooling at ~1000K/s (2 mm) and ~250K/s (4 mm).

When the molten material solidifies at ~1000K/s, the metastable B2 CuZr phase is mostly retained, as previously reported [52] but this cooling rate is not fast enough to prevent the crystallization of the more stable phases B19′ and the intermetallic multiphase (see XRD scans of

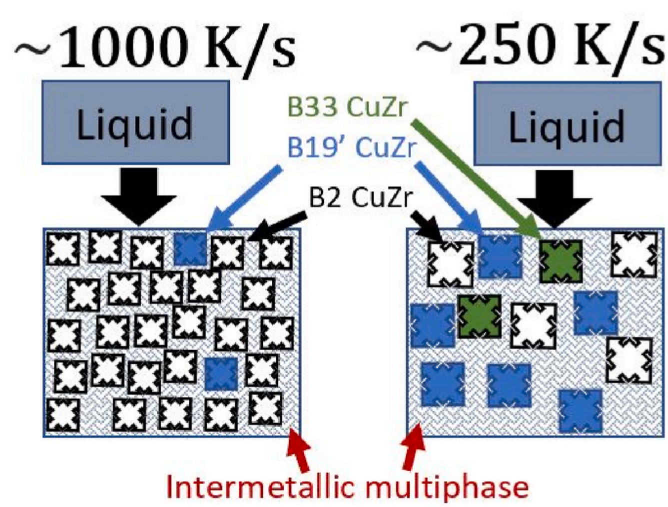

Fig. 10. Schematic of the microstructure for the two different cooling rates for the 2 mm (~1000K/s) and 4 mm (~250K/s) diameter samples.

Fig. 1a, c and e). However, at a cooling rate of ~250K/s the stable intermetallic multiphase dominates the microstructure followed by B19' and B33 martensites, although the more metastable B2 CuZr is still present (see XRD scans of Fig. 1b, d and f). The volume fractions of these phases, estimated from XRD results are summarized in Fig. 11, where the volume fraction of B2 CuZr phase is in the range 69–89% vol. for the 2 mm diameter sample while for the 4 mm diameter samples about 62–69% of the volume is the intermetallic multiphase [52,53] with some B2 CuZr austenite, from 13 to 18%, retained. In addition, the alloy with 0.5% Fe contains about 25% martensite by volume, most of which corresponds to the B33 phase, being responsible for the relatively low wear resistance of this alloy.

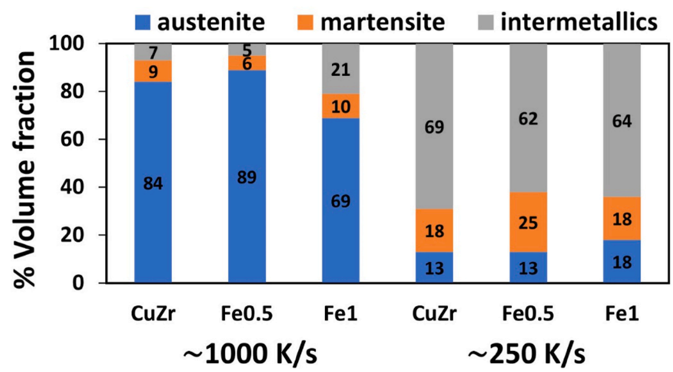

Fig. 11. vol fraction of austenite, martensite (B19′ and/or B33) and intermetallic phases for 2 mm (~1000K/s) and 4 mm diameter (~250 K/s) as cast $Cu_{50}Zr_{50}$, $Cu_{49.5}Zr_{50}Fe_{0.5}$, $Cu_{49}Zr_{50}Fe_{1}$ alloys.

5. Conclusions

The following conclusions can be drawn:

1. The combined effect of cooling rate (i.e., 2 mm and 4 mm diameter samples: ~1000 K/s and: ~250 K/s respectively) and microalloying with Fe (i.e., $Cu_{50}Zr_{50}$, $Cu_{49.5}Zr_{50}Fe_{0.5}$ and $Cu_{49}Zr_{50}Fe_{1}$) results in microstructural differences. For the highest cooling rate sample, the microstructure consists mostly of retained B2 austenite (from 68 to 89%) and microalloying does not have an appreciable effect on the microstructure. For the slowest cooling rate, the 4 mm diameter sample, the dominant phase is the intermetallic multiphase $Cu_{10}Zr_{7}$, $Cu_{8}Zr_{3}$ and $CuZr_{2}$ (from 64 to 69%) and addition of 0.5 at. % Fe promotes the formation of the more stable B33 CuZr phase.
2. The combined effect of cooling rate and microalloying affects the wear performance of $Cu_{50}Zr_{50}$, not only because of the differences in microstructure but also because Fe can enter into solid solution in the metastable B2 CuZr phase. For example, for the high cooling rate samples, despite the microstructure being basically the same for all compositions, the fact that 0.5 at. % Fe decreases the SFE of B2 phase and thus promotes the formation of B19′ martensite upon wear testing, improves the wear resistance of the alloy. However, for the low cooling rate samples, microalloying with 0.5 at. % Fe results in a large increase in volume fraction of B33 phase that decreases the wear resistance of the alloy. It is interesting to observe that there is no linear trend between the concentration in Fe and the stabilization of the B33 phase since for $Cu_{50}Zr_{50}$, and $Cu_{49}Zr_{50}Fe_{1}$ alloys the concentration of B33 phase is similar thus resulting in similar wear resistance.
3. Some differences in the wear mechanism are observed for 2 mm and 4 mm diameter samples. Although for both sample diameters it is observed that there are long continuous grooves induced by ploughing, a common feature of abrasive wear, but there are some differences. For the high cooling rate samples at 15 N load the signs of abrasive wear are relatively small while additional features consisting of subsurface cracks are observed. These features indicate that the wear mechanism is delamination characterized by the formation of lamellar wear debris. This is consistent with the relative low roughness of the wear surface, $R_a = 0.200$ μm, compared to the roughness for the low cooling rate samples for which only signs of abrasive wear are detected. This is especially true at the highest load of 40 N for which $R_a = 0.533$ μm since the presence of abundant $Cu_{10}Zr_{7}$, $Cu_{8}Zr_{3}$ and $CuZr_{2}$ hard intermetallic phases can form deep groves when they are dragged along the track.
4. From an engineering point of view, this paper demonstrates that proper selection of a microalloying element, its nature and concentration, is not enough to enhance the wear resistance of $Cu_{50}Zr_{50}$ SMA. Proper selection of the cooling rate upon casting is needed to guarantee success. Not only the cooling rate has to be fast enough to retain the microalloying element in solid solution, which also occurs in the 4 mm sample, but to prevent growth of undesirable phases. For example, as shown in this work, microalloying with 0.5 at. % Fe enhances the wear resistance when the cooling rate is ~1000 K/s but diminishes the wear resistance of the parent $Cu_{50}Zr_{50}$ alloy when the cooling rate is ~250 K/s. In this case, microalloying with the same element and concentration has a detrimental effect. Therefore, this should be taken into consideration at industrial scale during the fabrication process by using a suitable cooling system.

Data availability statement

The datasets generated during and/or analysed during the current study are available from the corresponding author on reasonable request.

Declaration of competing interest

The authors declare that they have no known competing financial interests or personal relationships that could have appeared to influence the work reported in this paper.

Acknowledgments

This work has been partially financed by the EPSRC through the ISCF North East Centre for Energy Materials (EP/R021503/1 (H G. and S.B.)) and the First Grant scheme (EP/P019889/1 (S.G.)). S.G. acknowledges this research contract from EPSRC. A. Younes acknowledges research support from Northumbria University.

References

[1] K. Otsuka, X. Ren, Prog. Mater. Sci. 50 (2005) 511.
[2] K. Otsuka, C. Wayman, Mechanism of shape memory effect and superelasticity, in: K. Otsuka, C.M. Wayman (Eds.), Shape Memorymaterials, Cambridge university press, 1998.
[3] S.A. Shabalovskaya, Bio Med. Mater. Eng. 12 (2002) 69.
[4] M. Kurumada, Y. Kimura, H. Suzuki, O. Kido, Y. Saito, C. Kaito, Scripta Mater. 50 (2004) 1413.
[5] K. Otsuka, C. Wayman, Shape Memory Materials, Cambridge university press, 1999, pp. 27–49.
[6] J. Ma, I. Karaman, R.D. Noebe, Int. Mater. Rev. 55 (2010) 257.
[7] Y. Zhang, X. Xu, Shape Mem. Superelasticity 6 (2020) 374.
[8] J.-X. Xie, J.-L. Liu, H.-Y. Huang, Rare Met. 34 (2015) 607.
[9] S. Pauly, J. Das, J. Bednarcik, N. Mattern, K.B. Kim, D.H. Kim, J. Eckert, Scripta Mater. 60 (2009) 431.
[10] C.A. Biffi, A. Figini Albisetti, A. Tuissi, Mater. Sci. Forum 738 (2013) 167.
[11] P. Nnamchi, A. Younes, S. González, Intermetallics 105 (2019) 61.
[12] Y. Miao, J.J. Vlassak, Acta Mater. 200 (2020) 162.
[13] F. De Luca, P. Nnamchi, A. Younes, A.T. Fry, S. González, J. Alloys Compd. 781 (2019) 337.
[14] Y. Wu, D.Q. Zhou, W.L. Song, H. Wang, Z.Y. Zhang, D. Ma, X.L. Wang, Z.P. Lu, Phys. Rev. Lett. 109 (2012), 245506-245501.
[15] M.L. Rahaman, L.C. Zhang, H.H. Ruan, Intermetallics 52 (2014) 36.
[16] M. Nishida, C.M. Wayman, T. Honma, Metall. Trans. A 17 (1986) 1505–1515.
[17] Y. Motemani, M. Nili-Ahmadabadi, M.J. Tan, M. Bornapour, S. Rayagan, J. Alloys Compd. 469 (2009) 164.

[18] R. Kainuma, M. Matsumoto, T. Honma, Bull. Res. Inst. Miner. Dressing Metall. 43 (1987) 149.
[19] H. Kozachkov, J. Kolodziejska, W.L. Johnson, D.C. Hofmann, Intermetallics 39 (2013) 89.
[20] F.A. Javid, N. Mattern, M.S. Khoshkhoo, M. Stoica, S. Pauly, J. Eckert, J. Alloys Compd. 590 (2014) 428.
[21] S. Pauly, G. Liu, G. Wang, J. Das, K.B. Kim, U. Kühn, D.H. Kim, J. Eckert, Appl. Phys. Lett. 95 (2009) 101906.
[22] S. Pauly, S. Gorantla, G. Wang, U. Kühn, J. Eckert, Nat. Mater. 9 (2010) 473.
[23] Y. Wu, Y. Xiao, G. Chen, C.T. Liu, Z. Lu, J. Adv. Mater. 22 (2010) 2770.
[24] A. Younes, P. Nnamchi, J. Medina, P. Pérez, V.M. Villapún, F. Badimuro, S. Kamnis, E. Jimenez-Melero, S. González, J. Alloys Compd. 817 (2020) 153330.
[25] C.A. Biffi, A. Figini, A. Tuissi, Intermetallics 46 (2014) 4.
[26] M.A. Chowdhury, D.M. Nuruzzaman, B.K. Roy, P.K. Dey, M.G. Mostafa, M.S. Islam, M.R. Mia, World Appl. Sci. J. 22 (2013) 1702.
[27] X. Lin, W. Johnson, J. Appl. Phys. 78 (1995) 6514.
[28] S.H. Zhou, R.E. Napolitano, Scripta Mater. 59 (2008) 1143.
[29] H. Baker, ASM handbook 3, 1992, pp. 2–80.
[30] J.D. Verhoeven, Fundamentals of Physical Metallurgy, Wiley, New York, 1975.
[31] V.M. Villapún, F. Esat, S. Bull, L.G. Dover, S. González, Materials 10 (2017) 506.
[32] L.M. Phinney, M.A. Spletzer, M.S. Baker, J.R. Serrano, J. Micromech. Microeng. 20 (2010), 095011.
[33] C.H. Ng, C.W. Chan, H.C. Man, D.G. Waugh, J. Lawrence, Surf. Coating. Technol. 309 (2017) 1015.
[34] J.F. Archard, J. Appl. Phys. 24 (1953) 981.
[35] L.J. Yang, Wear 259 (2005) 1453.
[36] R. Limbach, K. Kosiba, S. Pauly, U. Kühn, L. Wondraczek, J. Non-Cryst. Solids 459 (2017) 130.
[37] M.L. Rahaman, L. Zhang, M. Liu, W. Liu, Wear 332 (2015) 1231.
[38] N.P. Suh, Tribophysics, Pretice-Hall, Englewood Cliffs, New Jersey, 1986.
[39] V.M. Villapún, J. Medina, P. Pérez, F. Esat, F. Inam, S. González, Mater. Des. 135 (2017) 300.
[40] S. Prashantha, S.M. Shashidhara, U.S. Mallikarjun, A.G. Shivasiddaramaiah, Mater. Today 4 (2017) 10123.
[41] W.T. Qu, X.G. Sun, B.F. Yuan, K.M. Li, Z.G. Wang, Y. Li, Rare Met. 36 (2017) 478.
[42] H.C. Lin, J.L. He, K.C. Chen, H.M. Liao, K.M. Lin, Metall. Mater. Trans. 28 (1997) 1871.
[43] C. Taltavull, B. Torres, A.J. Lopez, J. Rams, Wear 301 (2013) 615.
[44] Y. Huang, H. Fan, D. Wang, Y. Sun, F. Liu, J. Shen, J. Sun, J. Mi, Mater. Des. 58 (2014) 284.
[45] P.J. Blau, R. Komanduri, J. Eng. Mater. Technol. 112 (1990) 254.
[46] J. Bhatt, S. Kumar, C. Dong, B.S. Murty, Mater. Sci. Eng. 458 (2007) 290.
[47] E. Hall, Proc. Phys. Soc. B 64 (1951) 747.
[48] Y. Yue, X. Zhang, J. Qin, R. Liu, J. Alloys Compd. 860 (2021) 157906.
[49] T. Zhao, Y. Li, Y. Liu, X. Zhao, J. Mech. Behav. Biomed. Mater. 13 (2012) 174.
[50] Y. Li, F. Zhang, T.T. Zhao, M. Tang, Y. Liu, Rare Met. 33 (2014) 244.
[51] S. Waqar, A. Wadood, A. Mateen, M.A.U. Rehman, Int. J. Adv. Manuf. Technol. 108 (2020) 625.
[52] F.A. Javid, N. Mattern, M.S. Stoica, S. Pauly, J. Eckert, J. Alloys Compd. 590 (2014) 428.
[53] X. Cui, F.Q. Zu, Z.Z. Wang, Z.Y. Huang, X.Y. Li, L.F. Wang, Intermetallics 36 (2013) 21.